Aerodynamic Design of a Martian Micro Air Vehicle

T. Désert *, J.M. Moschetta, and H. Bézard
ONERA and ISAE-SUPAERO

ABSTRACT

The present study aims at developing a reliable propulsion system for a rotary wing micro air vehicle (MAV) associated to rovers in order to enhance Martian exploration rate. The main challenge encountered for MAV design is Martian atmosphere's density and speed of sound that are significantly lower than on Earth. Leading to compressible ultra low Reynolds number ($2,000 < Re_{dom} < 10,000$) flows met at blades tip that are unusual and unknown in the biosphere. Consequently, evaluations of numerical tools have been carried out recreating a depressurized experiment. 2D and 3D steady and unsteady Navier-Stokes computations are compared to XFoil for flow behavior apprehension and solver assessment. Based on XFoil's performances evaluations, camber line and thickness distribution have been optimized for 2D incompressible and compressible flows. Optimal shape for a steady solver is a highly cambered airfoil shifting the boundary layer separation downstream. 2D unsteady Navier-Stokes computations show that airfoils delaying heavy unsteadiness generation are producing higher lift and lower drag in 2D than the picked airfoils enhancing vortex production, such as dragonfly airfoils. The impact of airfoil shape on 3D flows is evaluated with a first of its kind experimental campaign in collaboration with CNES. The experimental facility is a ONERA's $18m^3$ tank recreating Martian atmosphere in terms on kinematic viscosity and composition. The tank size allows to reduce wall effects and provide - as compared to previous studies - a more accurate evaluation of rotor performances.

1 INTRODUCTION

Since 2004, three exploration rovers have successfully landed on the Martian surface. Yet, only about sixty kilometers have been explored on 21,000 km of the planet's circumferential path. The slow exploration rate is mainly due to a lack of visibility on the ground. A rotary wing micro air vehicle (MAV) associated to rovers could significantly increase their mobility by providing an aerial point of view of their upcoming pathway. However, Martian atmosphere is far from MAV friendly: density is hundred times lower than on Earth and speed of sound is also lower due to low temperature and different atmosphere composition (96% of CO_2). Hence, a new aerodynamic domain is explored: compressible ultra low Reynolds number flows - Table 1.

	Earth	**Mars**
Density (kg/m^3)	1.225	0.014
Dynamic viscosity (mPa.s)	0.0181	0.0106
Average temperature ($^\circ$C)	15	-63
Speed of sound (m/s)	340	238

Table 1: Atmospheric conditions of Mars and the Earth at ground level

So far, the very few papers operating in this Reynolds number range are mostly studying the impact of Reynolds number [1] and turbulence rate [2] on flow laminarity or evaluating aerodynamic performances of typical airfoils [3] and planform distributions [4]. Only two studies provide airfoil camber line optimization at $Re_c = 6,000$ [5] and $6,000 < Re_c < 16,000$ [6] for incompressible flows. Neither thickness distribution nor compressible optimization have been undertaken yet. Incompressible experimental devices are usually low speed wind tunnels [1], water tunnels [2][3] or nanorotors [5][6]. As far as we know, only two depressurized experiments recreate compressible ultra-low Reynolds number conditions for airfoil [7] or rotor [8] performances measurement. However, neither studies provide a validated computational tool for flow simulation. In the present study, a computational tool is validated on compressible ultra low Reynolds number flows. Moreover, incompressible and compressible airfoil optimizations of both camber line and thickness distributions are carried out. The optimized airfoils are evaluated and compared to airfoils from literature with the validated solver and an experimental campaign.
This paper presents an aerodynamic design of a MAV operating in Martian atmosphere. First, MAV's flight conditions domain is defined. In this domain, steady and unsteady numerical tools are evaluated and compared to *Mars Wind Tunnel* experiment [7]. Then, a compressible airfoil shape optimization process based on 2D steady performances is characterized and carried out step by step for flow behavior apprehension. Finally, the impact of airfoil shape on rotor performances is evaluated thanks to a first of its kind experimental campaign recreating Martian atmospheric conditions and gas composition in an $18m^3$ tank.

*Email address: thibault.desert@onera.fr

2 Description of Martian Micro Air Vehicle flight conditions

Aerodynamic design's domain of the rotary wing MAV correspond to the MAV's flight conditions in hover: Reynolds Number and Mach number range. These two dimensionless quantities depend on atmospheric conditions, MAV's size, weight and rotational speed. The constraints are the diameter of the MAV around 30 cm, its weight of about 200 g and the maximum rotational speed set to avoid locally supersonic flow.

2D laminar steady Navier-Stokes computations set maximal subsonic rotational speed to $12,000$ rpm corresponding to $M = 0.8$ at blade's tip for $c = 238m.s^{-1}$ ($T = -63°C$). Chord Reynolds number range is determined via BEMT evaluations with a number of blades range $n_{blades} \in [\![2, 5]\!]$: $2,000 < Re_{dom} < 10,000$. The upper boundary of the Reynolds number range is enhanced in case of heavier MAV design. The reference Reynolds number is: $Re_{ref} = 3,000$.

3 Assessment of 2D and 3D numerical tools for compressible ultra-Low Reynolds number flows

Numerical tools are not validated on compressible ultra-Low Reynolds number flows yet. Solvers need to be evaluated and compared to an experiment recreating Martian atmospheric conditions : the *Mars Wind Tunnel* [7]. The unsteady solver, elsA [9], is validated on a 3D simulation recreating the test section. The steady quick solver, XFoil, is assessed for a purpose of airfoil optimization process.

3.1 Tohoku's University Mars Wind Tunnel experiment [7]

The *Mars Wind Tunnel* (MWT) experimental device is located at Tohoku's University - Figure 1. It consists of a wind tunnel reproducing Martian atmospheric composition: density and gas. We evaluated the case of the triangular airfoil [7]. This airfoil's strong leading edge camber and sharpness causes significant unsteadiness in the flow, making it interesting for numerical validation. Low density allows to reach

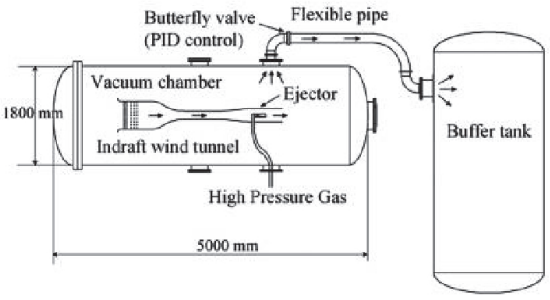

Figure 1: Tohoku's University *Mars Wind Tunnel* experiment

$Re_c = 3,000$ for different Mach numbers - $M = 0.15$ & 0.5. Forces are measured with a balance and pressure distributions are available on the upper part of the airfoil thanks to pressure sensitive paint (PSP). Even if the MWT experiment is supposed to recreate 2D flows, PSP measurement showed a three dimensionality over the airfoil. Moreover, author's 3D LES computations [7] provide greater lift and drag predictions than the experiment while not taking into account the test sections - Figure 2. This phenomenon is due to wall effect on the sides on the test section: the entire experiment needs to be simulated for proper flow and forces evaluations.

3.2 3D unsteady Navier-Stokes solver elsA

The solver elsA was developed by ONERA in the 90's. It is based on an integral form of the compressible Navier-Stokes equations [9]. Considering the Reynolds number range, the hypothesis of laminar flow in a non turbulent environment is conceivable. Transition criteria, such as AHD and Moore, have preliminary confirmed that no transition would occur neither by amplification of Tollmien-Schlichting waves nor by separation bubble. Mesh convergence has been studied for all Navier-Stokes simulations.

3D unsteady simulations recreating the MWT test section are needed in order to recreate the same test conditions as in the experiment. Representative flow conditions ($Re_c = 3,000$, $M = 0.5$) are chosen. $117,000$ cells 2D H-topology meshes with 242 nodes mapping the airfoil's upper surface and 151 for the lower surface have been made taking into account the test section walls with different angles of attack of the airfoil: $5°$, $10°$ and $15°$. The first cell height is set to 2.10^{-4} for chord-normalized coordinate system. From those 2D meshes, 15 millions cells 3D meshes have been constructed with 131 nodes in spanwise direction for a width of 3.3c. As presented

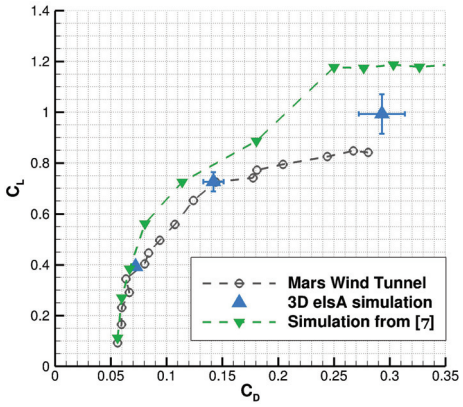

Figure 2: Polar comparing MWT, 3D computations from [7] and 3D elsA simulation (with standard deviation) ($Re_c = 3,000$, $M = 0.5$)

in Figure 2, laminar unsteady Navier-Stokes solver accurately predicts the 3D forces generated at the two first angles of attack ($5°$ and $10°$). However, for the third angle of attack, corresponding to a fully detached flow, computed lift is over-

estimated. Since we do not intend to evaluate highly perturbed environment, we consider the solver validated for 3D flows and by extension, we assume that it provides reliable 2D flow predictions.

3.3 2D steady solver assessement for airfoil optimization process

In an airfoil optimization process, a quick and effective tool is needed for performances comparison: unsteady Navier-Stokes simulations' computational cost is too significant. XFoil, a potential flow solver strongly interacted with integral boundary layer formulation, provides a quick steady evaluation of lift, drag and boundary layer state. In order to evaluate laminar XFoil forces prediction, we compare it to laminar steady and unsteady elsA solver on the triangular airfoil test case ($Re_c = 3,000$, $M = 0.5$). Mesh used for these elsA evaluations counts $89,200$ cells with 242 nodes mapping the upper surface and 151 for the lower surface. It is noted that XFoil provides a Karman-Tsien compressibility correction for C_P and external velocity u_e. The integral boundary layer formulation is already valid for compressible flow, therefore, it may be considered as a subcritical compressible solver. As we observe in Figure 3(a), taking into account

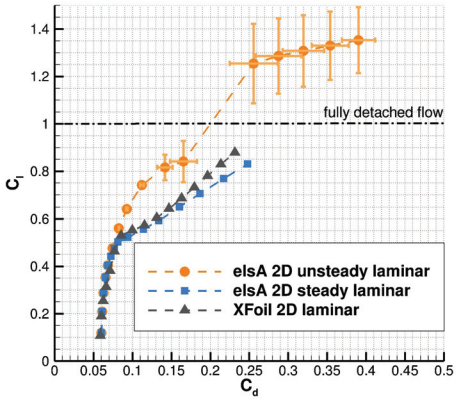

(a) Polar comparing elsA steady and unsteady 2D simulations (with standard deviation) and XFoil ($Re_c = 3,000$, $M = 0.5$)

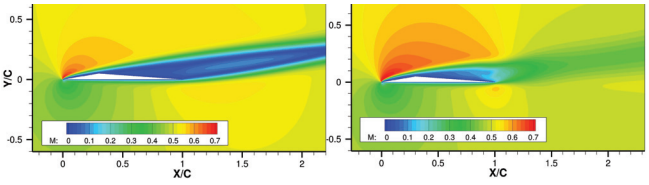

(b) Mach fields in steady case (left) and averaged unsteady (right) ($Re_c = 3,000$, $M = 0.5$, $\alpha = 9°$)

Figure 3: Comparison of different 2D solvers on compressible ultra-low Reynolds number flows

unsteadiness in 2D compressible ultra-low Reynolds number simulations increases the forces generated by the airfoil. This is due to the recirculation zone created by boundary layer separation. For $C_l < 1$, detachment is triggered by 0.3c upper surface discontinuity - Figure 3(b). For $C_l > 1$, flow is fully detached from leading to trailing edge creating a lift and drag overshoot going along with strong unsteadiness. In steady computations using XFoil and elsA, boundary layer separation creates a massive drag rise without significant lift gain causing poor aerodynamic performances. However, forces predictions anterior to heavy boundary layer separation provide valuable hint on airfoil's performances. Therefore, we consider that we can use the steady solver XFoil for airfoil comparison in an optimization process acknowledging that it does not take on board the entire physic of the flow.

4 AIRFOIL OPTIMIZATION PROCESS BASED ON XFOIL'S PERFORMANCES EVALUATIONS

In a purpose of optimization, automatic airfoil generation with finite parameters is primordial. CST method [10] has been chosen because of its ability to recreate any $\mathcal{C}^2$ continuous airfoil shapes with a restricted number of parameters. In this study, we used five parameters to reflect the shape of one curve: camber or thickness distribution. Note that discontinuous airfoils, for example corrugated airfoils, cannot be represented with this parametrization method. However, XFoil is not able to simulate a recirculation zone in a corrugation. The major issue raised by XFoil is convergence: many phenomenon can cause a non-convergence compelling the optimization process to be extremely robust to it. The optimization process consists of evaluating the entire parameters domain with an increasing proximity between the different sets of parameters. As presented in Figure 4, from each input generation N, ten sets of parameters are selected as the most effective airfoils by a performance function. The sets of parameters outside of the zone created by the ten selected are eliminated from the optimization domain: a new domain is formed and a new input generation $N + 1$ is evaluated. Since Martian atmosphere is highly turbulent, the blade's flight conditions can fluctuate. Hence, performance function needs to evaluate the airfoil's competitiveness in the entire hover range of a Martian micro air vehicle. Each set of parameters, representing an airfoil shape, is evaluated on three Reynolds numbers representative of the entire Martian MAV flight domain: $Re_c \in (2,000; 6,000; 10,000)$. The performance function is built as the mean value between lift-to-drag ratio and endurance coefficient over the range of Reynolds numbers and a range of angles of incidence. The process is robust to non-convergence because it does not learn from previous evaluations: we observe an unconverged set of parameters from generation N represented with a green triangle - Figure 4. Since its set of parameters is part of the zone formed by the most effective airfoils of its generation, it is still part of the new generation domain and a close set of parameters is going to be evaluated and converged. However, sufficient proximity on the domain is needed in order to avoid the elimination of

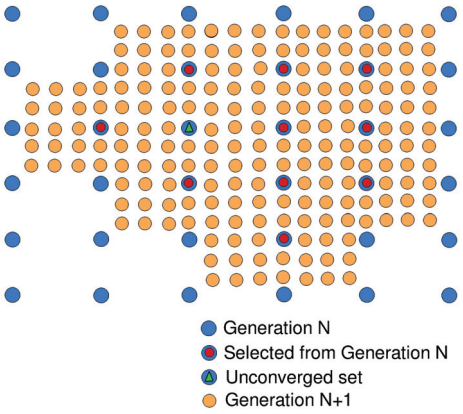

Figure 4: 2D representation of selection process robust to non-convergence

unconverged effective sets of parameters: it demands a very important number of sets and a parallelized process. Each generation counts at least $50,000$ sets of parameters evaluated several times for each of the three Reynolds numbers. Approximately half a million XFoil evaluations are carried out in each generation.

5 Results of compressible and incompressible airfoil optimization for ultra-low Reynolds number flows

We acknowledge that heavy boundary layer separations are causing poor aerodynamic performances or non-convergence in XFoil. Hence, airfoils enhancing vortex production cannot be truly evaluated and the optimization process aims at generating airfoils shifting the boundary layer separation downstream. For flow behavior apprehension, optimization has been carried out step by step, adding gradual complexity in incompressible flows and then assessing the impact of compressibility.

5.1 Incompressible airfoil shape optimization: camber line and thickness distribution

In the study, three incompressible optimization process have been carried out. Camber line optimization with a prescribed 2% relative thickness distribution having round leading edge and sharp trailing edge. Then, thickness distribution optimization from optimal camber line with a minimum relative thickness constraint set to $T_{min} = 1\%$. Finally, since camber line and thickness distribution are co-dependent, general airfoil shape optimization. As presented in Figure 5(a), camber line shape of each step's optimal airfoils follows the same pattern: a cambered leading edge for proper flow adaptation avoiding early boundary layer separation. A slightly tilted flat middle shape permitting to delay boundary layer detachment. And the highly cambered trailing edge fixes the separation point. Hence, optimal airfoils are producing sufficient lift with high camber while shifting the boundary layer separation downstream. The two incompressible camber line optimizations from literature provide the same general camber line shape for similar range of Reynolds number [5][6]. Optimized thickness distributions show a thin leading edge for proper flow adaptation and a surprising round trailing edge: its impact is evaluated in section 6.2. The optimized thickness distribution with a pre-optimized camber line displays thinner parts at $x/c = 0.15$ & 0.8 that are no longer present with the general shape optimization. Thickness distribution optimization is compensating for the over-cambered line designed for the prescribed leading edge and trailing edge distributions. Figure 5(b) exhibit a better lift-to-drag ratio on a wider range of coefficient of lift at each optimization complexity increment. This is due to better leading edge flow

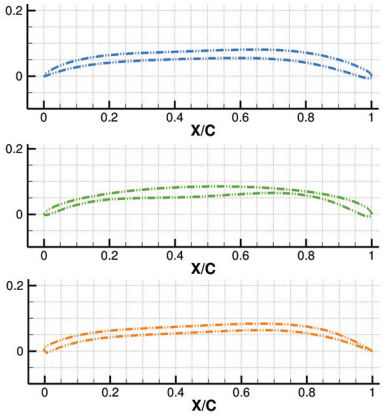

(a) Incompressible XFoil optimal airfoil shapes: camber line optimization with a predefined thickness distribution (yellow), thickness distribution optimization (green) and general shape optimization (blue)

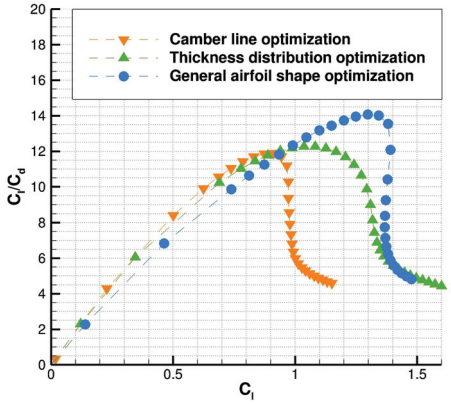

(b) XFoil's lift-to-drag ratio in flight conditions ($Re_c = 6,000$, $M = 0.1$)

Figure 5: Incompressible general airfoil optimization performances comparison with the different optimization steps

adaptation and trailing edge decompression permitting wider pressure distributions.

5.2 Compressible airfoil shape optimization: camber line and thickness distribution

The impact of compressibility has been evaluated for the general airfoil shape optimization. We remind that XFoil may be considered as a compressible solver for subsonic flows: flow rate is set to $M = 0.5$ for avoiding local shocks appearance. As presented in Figure 6, compressible airfoil optimization results in an equivalent thickness distribution with a reduced camber compared to incompressible optimization. In compressible flows, boundary layer separation is more easily triggered: the reduced camber permits to delay high drag production at higher lift, hence, a better lift-to-drag ratio is achieved.

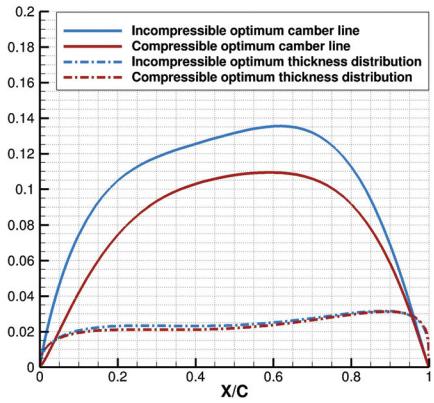

Figure 6: General airfoil shape comparison for a compressible and incompressible optimization

6 Evaluation of the optimized airfoils compared to airfoils picked from literature in 2D unsteady compressible Navier-Stokes simulations

Since the optimization process is based on a simplified steady solver performances evaluations, it is essential to numerically audit the optimal airfoils with a validated solver.

6.1 Assessment of the optimized airfoils in compressible ultra-low Reynolds number flows

Figure 7 exhibits the aerodynamic performances of each optimization steps' optimal airfoil in compressible ultra low Reynolds number flows. They have very close unsteady Navier-Stokes lift-to-drag ratio and tendencies are the same for each Reynolds number of the Martian MAV's range. Compressible optimum generates lower drag for $C_l < 1$ than more highly cambered optimized airfoils. However, more highly cambered airfoils suffer the drag rise at higher lift generation. Therefore, the 2D optimal camber line depends on

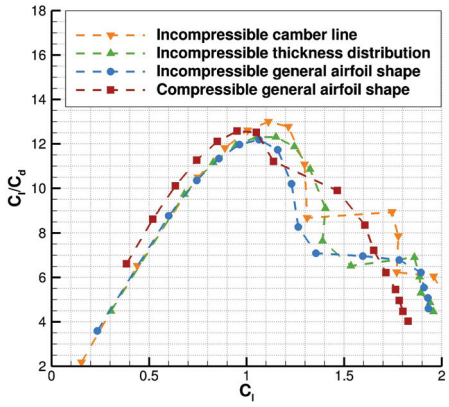

Figure 7: Averaged unsteady 2D N-S lift-to-drag ratio of the optimized airfoils evaluated with elsA in flight conditions ($Re_c = 6,000$, $M = 0.5$)

the aimed range of lift coefficient. We also note that the incompressible camber line optimization provides the best lift-to-drag ratio. It means that thickness distribution optimization for a given camber line did not enhance 2D unsteady aerodynamic performances.

6.2 Impact of round trailing edge on aerodynamic performances

The main difference between the optimized and the prescribed thickness distribution comes from trailing edge definition, therefore, we intend to evaluate the impact of this difference by producing an optimal compressible airfoil with a sharp trailing edge replacing its unusual round shape. As presented in Figure 8, gap in 2D aerodynamic performances for different trailing edge thickness distributions is minor. Considering the Reynolds number range, boundary layer growth

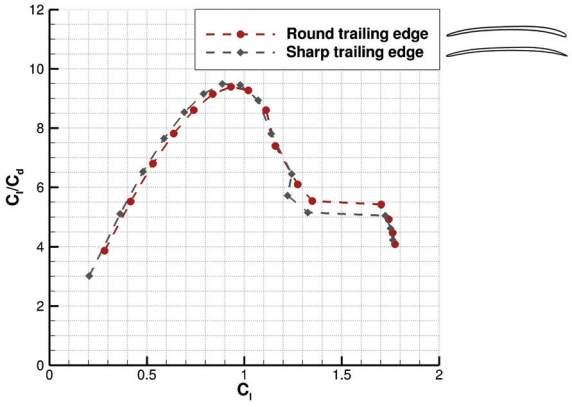

Figure 8: Evaluation of the impact of round trailing edge on aerodynamic performances: averaged unsteady N-S polar in flight conditions ($Re_c = 3,000$, $M = 0.5$)

and the recirculation zone triggered by separation at upper surface minimize the magnitude of trailing edge shape. Therefore, in Figure 7, the difference in performances between the incompressible camber line and the incompressible thickness distribution mainly comes from leading edge definition.

6.3 *Compressible and incompressible evaluation of a steady optimized airfoil compared to airfoils picked from literature*

Since the optimized airfoils were build relying on a steady process, we compare the compressible general airfoil shape to airfoils considered in the literature as effective in ultra low Reynolds number flows. The 6% cambered plate has been proven experimentally to be the most effective of the tested airfoil for Martian flight conditions [5][4]. And since biomimicry tends to drive us toward corrugated airfoils enhancing vortex production, a dragonfly airfoil - Figure 10(b) - is picked: it was also experimentally proven to be the most aerodynamically effective from three sections at different radius of a dragonfly wing at ultra-low Reynolds number [11]. Both airfoils are generated with a 2% relative thickness distribution. We observe in Figure 9 that airfoils delaying boundary layer separation provide far better 2D unsteady Navier-Stokes lift-to-drag ratio in ultra-low Reynolds number flows than the dragonfly airfoil. We note that performances are very similar in compressible and incompressible flows for low lift production. At higher lift production, drag rise is more important in compressible flows. Hence, for robustness, design C_l in rotor generation has to be weakened. Figure 10 displays the averaged mach number contours for a production of $C_l \sim 0.85$ of the compressible optimal and the dragonfly airfoil. The corrugated airfoil triggers boundary layer detachment early in chordwise direction degrading 2D performances. However, we acknowledge that only one corrugated airfoil has been computed.

To conclude, XFoil provides valuable hints on airfoil performances permitting to figure out trends in airfoil shapes optimization. 2D unsteady Navier-Stokes evaluations do not show large differences in performances for airfoils postponing boundary layer separation. Nevertheless, a slight 2D performances enhancement could have a greater impact on 3D flows.

7 Experimental campaign in a depressurized facility recreating Martian atmospheric conditions

Because flow behaviors might be very different in a 3D rotary system compared to 2D computations, an experimental campaign in a depressurized tank has been carried out in collaboration with CNES. The purposes of the campaign are to understand the flows encountered by experimental rotors and to evaluate the impact of airfoil shape and gas composition on rotor performances.

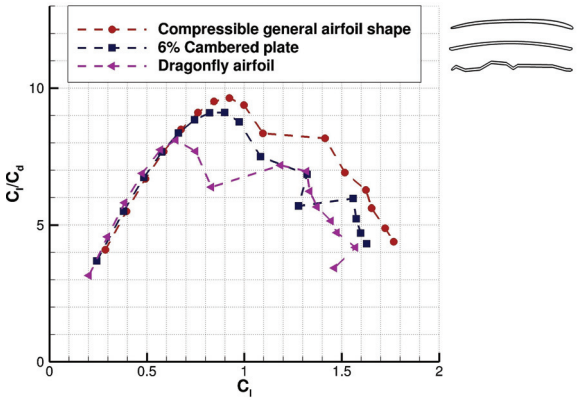

(a) Incompressible averaged unsteady N-S polar in flight conditions ($Re_c = 3,000$, $M = 0.1$)

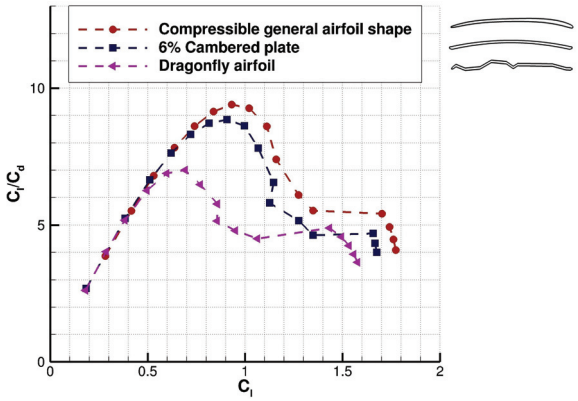

(b) Compressible averaged unsteady N-S polar in flight conditions ($Re_c = 3,000$, $M = 0.5$)

Figure 9: Incompressible and compressible 2D aerodynamic performances evaluated with elsA of an optimized airfoil compared to airfoils from literature [11][5][7]

7.1 *Experimental setup and rotor production*

The depressurized facility is a 18 m^3 tank located at ONERA's Fauga center. Inside the tank, an ISAE-SUPAERO testbed is incorporated for thrust and torque measurement - Figure 11. Note that rotor wake heads toward tank's tube, significantly reducing flow recirculation. Martian atmospheric conditions are met in the tank in terms of kinematic viscosity for flight Reynolds number consistency with the two different gases: Air and CO_2 (96%). The aimed pressure inside the tank has been calculated from temperature and gas composition. Hence, performances are compared with dimensionless numbers:

$$C_T = \frac{T}{\rho A(\Omega R)^2} \qquad C_P = \frac{P}{\rho A(\Omega R)^3} \tag{1}$$

Experimental rotors have the same planform distribution from Maryland's experiment [8] - Figure 12. Four airfoil shapes

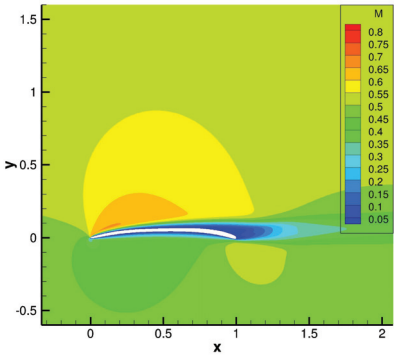

(a) Averaged unsteady N-S mach fields in flight conditions ($Re_c = 3,000$, $M = 0.5$, $\alpha = 5°$) for the compressible general airfoil shape

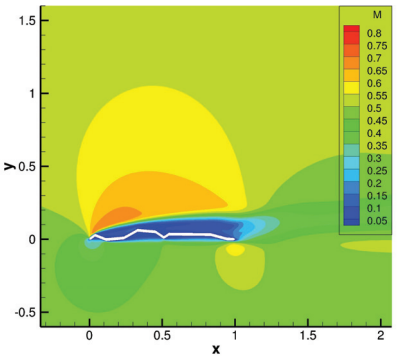

(b) Averaged unsteady N-S mach fields in flight conditions ($Re_c = 3,000$, $M = 0.5$, $\alpha = 7°$) for the dragonfly airfoil

Figure 10: 2D averaged unsteady N-S mach fields evaluated with elsA

(a) ISAE-SUPAERO's experimental testbed in the depressurised tank

(b) 18 m^3 depressurized tank located at ONERA's Fauga center

Figure 11: Experimental facility evaluating rotor performances in Martian atmosphere

are evaluated: Maryland's airfoil (6.35% cambered plate), compressible optimum with round and sharp trailing edge and finally the dragonfly airfoil. Rotors and hubs are produced with a liquid resin printer except from the rotor with Maryland's airfoil that was built in carbon.

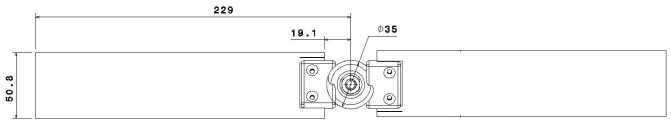

Figure 12: Experimental rotors' planform distribution [8] for evaluating the impact of airfoil shape on rotor performances

7.2 *Rotor performances in Martian atmospheric conditions and gas composition*

Every experimental rotor has been evaluated in Air and CO_2. Dimensionless performances are comparable in both cases [7] and differences are within the measurement uncertainty. We chose to show the rotor performances in CO_2 since it is closer from Martian atmosphere. Figure 13 displays thrust coefficient of experiments from ONERA and Maryland [8] for different collective pitch angles. Maryland's efforts are under-estimated compared to ONERA's: this is certainly due to flow recirculation inside the smaller tank (0.6 m^3). However, tendencies are comparable thus a correction for compensating the recirculation might be contemplated. For 3D ultra-

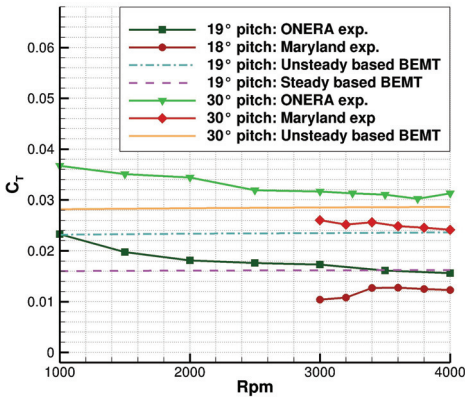

Figure 13: Coefficient of thrust from ONERA and Maryland experiments compared to 2D unsteady and steady based BEMT computations

low Reynolds number flow physics apprehension, Figure 13 also shows expectations from BEMT computations based on 2D unsteady and steady Navier-Stokes polars. For a 19° collective pitch, measured thrust is close to steady based BEMT. However, for a 30° collective pitch, it is closer to unsteady based BEMT than steady based BEMT. Our hypothesis is

that centrifugal forces might tend to stabilize the unsteady flow over the rotor's blades. But, this phenomenon would not be important enough to stabilize a highly unsteady flow at 30° collective pitch. Unsteady CFD rotor computations are in progress for a better understanding of 3D flows encountered by Martian rotors.

The impact of airfoil shape on 3D flows is studied in Figure 14. Rotor performances show the same tendencies as in 2D Navier-Stokes computations for the different airfoil shapes. Highly cambered airfoils shifting boundary layer separation downstream show comparable C_T/C_P and thrust range while the dragonfly airfoil displays poor performances and thrust range. Hence, dragonfly wings are not optimized for gliding at ultra-low Reynolds number.

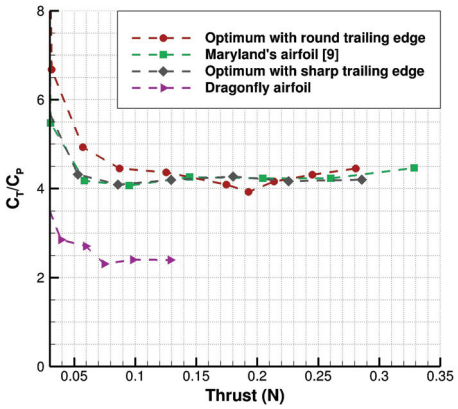

Figure 14: Impact of airfoil shape on rotor performances in CO_2 for the same planform distribution - Figure 12 - and a collective pitch angle of 19° $(1,000 < Rpm < 4,000)$

8 Conclusion

The main conclusions drawn on 2D and 3D compressible ultra-low Reynolds number flows during this numerical and experimental study are the following:

- Laminar unsteady Navier-Stokes solver elsA provides a proper flow simulation and forces prediction in an undisturbed 3D environment.
- 2D steady computations allow to assess the incidence of boundary layer separation and to provide valuable hints on airfoil performances. Making them useful tools for airfoil optimization.
- Effective airfoils for 2D ultra-low Reynolds number flows are highly cambered airfoils with leading edge and trailing edge camber allowing to delay boundary layer separation and unsteadiness production.
- Subcritical compressibility has little impact on 2D aerodynamic performances but eases boundary layer detachment.
- Rotor dimensionless performances are comparable with an Air or CO_2 filled tank for the same flight Reynolds number.
- Tendencies between airfoils performances in experimental campaign recreating Martian flight conditions are the same as with 2D laminar Navier-Stokes computations.

References

[1] R. W. Derksen, M. Agelinchaab, and M. Tachie. Characteristics of the flow over a naca 0012 airfoil at low reynolds numbers. *WIT Transactions on Engineering Sciences*, 2008.

[2] S. Wang, Y. Zhou, and Md. Alam. Effects of reynolds number and turbulent intensity on a low reynolds number airfoil. *AIAA Aviation*, 2014.

[3] S. Sunada, T. Yasuda, and K. Yasuda ans K. Kawachi. Comparison of wing characteristics at an ultralow reynolds number. *Journal of Aircraft*, 2002.

[4] F. Bohorquez. *Rotor Hover Performance and System Design of an Efficient Coaxial Rotary Wing Micro Air Vehicle*. PhD thesis, University of Maryland, 2007.

[5] P.J. Kunz. *Aerodynamics and Design for Ultra-Low Reynolds number flight*. PhD thesis, University of Stanford, 2003.

[6] Z. Liu, L. Dong, J.M. Moschetta, J. Zhao, and G. Yan. Optimization of nano-rotor blade airfoil using controlled elitist nsga-ii. *International Journal of Micro Air Vehicles*, 2014.

[7] P.M. Munday, K. Taira, T. Suwa, D. Numata, and K. Asai. Nonlinear lift on a triangular airfoil in low-reynolds-number compressible flow. *Journal of Aircraft*, May-June 2015.

[8] R. Shrestha, M. Benedict, V. Hrishikeshavan, and I. Chopra. Hover performance of a small-scale helicopter rotor for flying on mars. *Journal of Aircraft*, 2016.

[9] L. Cambier, M. Gazaix, S. Heib, S. Plot, M. Poinot, J.P. Veuillot, J.F. Boussuge, and M. Montagnac. An overview of the multi-purpose elsa flow solver. *Journal Aerospace Lab*, 2011.

[10] B.M. Kulfan and J.E. Bussoletti. "fundamental" parametric geometry representations for aircraft component shapes. In *11th AIAA/ISSMO Multidisciplinary Analysis and Optimization*, 2006.

[11] A. Kesel. Aerodynamic characteristics of dragonfly wing sections compared with technical aerofoils. *The Journal of Experimental Biology*, 2000.